A face-regulated tetrahedral cage for selective and efficient encapsulation of perylene dimers

Haiying Wang,[a] Wenbin Zhong,[b] Wei Yuan,[d] Guoqiang Jiang,[c] Andrew C.-H. Sue [c] and Wangjian Fang*[c,d]

[a]Medical Imaging Key Laboratory of Sichuan Province, North Sichuan Medical College, Nanchong, Sichuan Province 637000, P. R. China.

[b]School of Food Science and Technology, Nanchang University, Nanchang, Jiangxi Province 330047, P. R. China.

[c]College of Chemistry and Chemical Engineering, Xiamen University, Xiamen, Fujian Province 361005, P. R. China.

[d]Department of Chemistry, National University of Singapore, Singapore 117543, Singapore.

E-mail: wjfang@tju.edu.cn

Contents

Materials and Methods

Reagents, solvents, and initial substances were acquired from commercial sources and utilized in their original form unless specified otherwise. Silica gel of 200-300 mesh or 300-400 mesh sizes was used for conducting flash column chromatography. ^{1}H, ^{19}F, ^{13}C NMR, COSY, NOESY and DOSY spectra were conducted on either a Bruker Avance 400 MHz or a 600 MHz NMR spectrometer or a JEOL ECA 500 NMR Spectrometer, with measurements taken at room temperature. Reported chemical shifts are given in parts per million (ppm) on the δ scale, with scalar coupling constants denoted in Hz. The spectral chemical shift referencing was standardized against TMS as an internal reference, with a chemical shift of δ 0.0 ppm, except where specified otherwise. High-resolution mass spectra (HRMS) of ligands were measured on a high resolution mass spectrometer equipped with Waters Acquity UPLC. Waters Xevo G2-X2 MS enables automated exact mass measurements. High-resolution mass spectrometric analyses of assemblies were performed on a QExactive™ HF Hybrid Quadrupole-Orbitrap Mass Spectrometer interfaced with an UltiMate™ 3000 RSLCnano system, equipped with a Nano ProFlow meter operating with ProFlow technology for enhanced flow precision and sensitivity. TEM was performed on FEI Tecnai G2 F20 Field emission transmission electron microscope. Fluorescence spectra and time–dependent luminescence decays were performed with FLS980 full–featured fluorescence spectrometer. UV–Vis spectra was performed on Agilent Cary 60 UV–visible spectrophotometer. EPR spectra were measured on a Bruker EMX plus spectrometer. Fluorescence imaging experiment was performed on Zeiss LSM 800 Confocal Microscope.

Synthetic Procedure

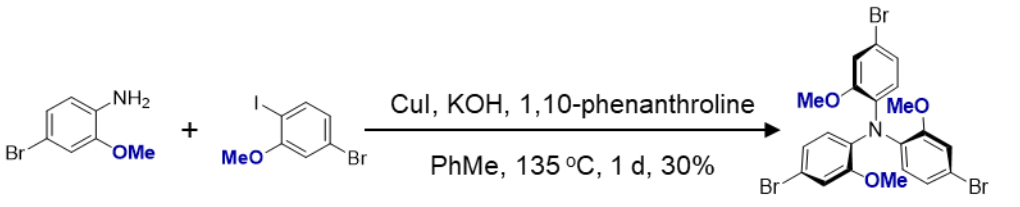

tris(4-bromo-2-methoxyphenyl)amine

Synthesis of tris(4-bromo-2-methoxyphenyl)amine: In a typical experiment, a mixture of 4-bromo-2-

methoxyaniline (5.20 g, 26 mmol), 4-bromo-1-iodo-2-methoxybenzene (18.00 g, 58 mmol), CuI (1.53 g, 8 mmol), 1,10-phenanthroline (0.96 g, 5.28 mmol) and potassium hydroxide (11.8 g, 210 mmol) were dissolved in 120 mL of toluene and stirred under a nitrogen atmosphere at reflux for 24 h. At the end of reaction, the mixture was then cooled to RT and poured into distilled water. The products were extracted using CH_2Cl_2 and the organic layer was dried over anhydrous sodium sulphate. The solvent was meticulously depleted utilizing a reduced pressure technique, subsequently providing crude compounds. These were then subjected to a purification process via silica gel short column chromatography using *n*-hexane/EtOAc (20/1 to 12/1) to afford **tris(4-bromo-2-methoxyphenyl)amine** as a yellow solid in 30% yield. ^{1}H NMR (500 MHz, $CDCl_3$) δ 6.94 (d, J = 2.1 Hz), 6.90 (dd, J = 8.4, 2.2 Hz), 6.62 (d, J = 8.4 Hz), 3.56. ^{13}C NMR (100 MHz, $CDCl_3$) δ 153.5, 135.8, 125.4, 123.7, 116.8, 115.8, 56.0. HRMS (ESI) *m/z* $[M + H]^+$ Calcd for $C_{21}H_{19}Br_3NO_3$ 571.8889, found 571.8797.

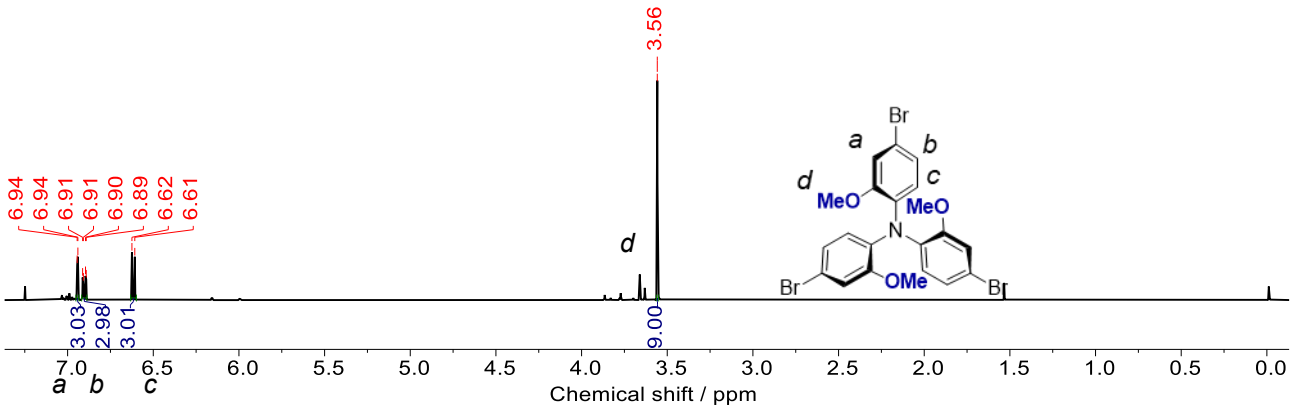

Figure S1. ^{1}H NMR spectrum of **tris(4-bromo-2-methoxyphenyl)amine** (400 MHz, $CDCl_3$, 298 K).

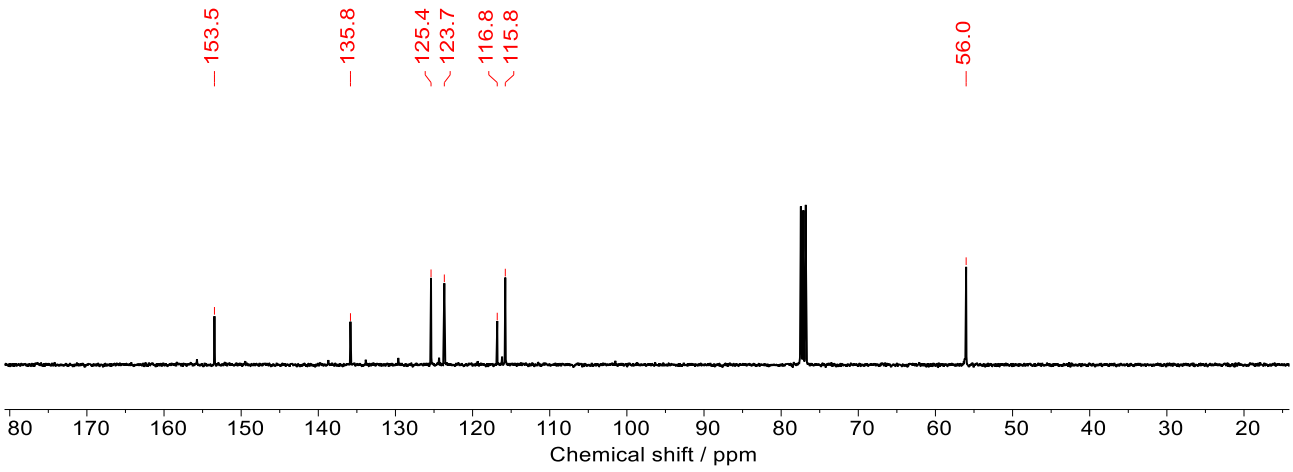

Figure S2. ^{13}C NMR spectrum of **tris(4-bromo-2-methoxyphenyl)amine** (101 MHz, $CDCl_3$, 298 K).

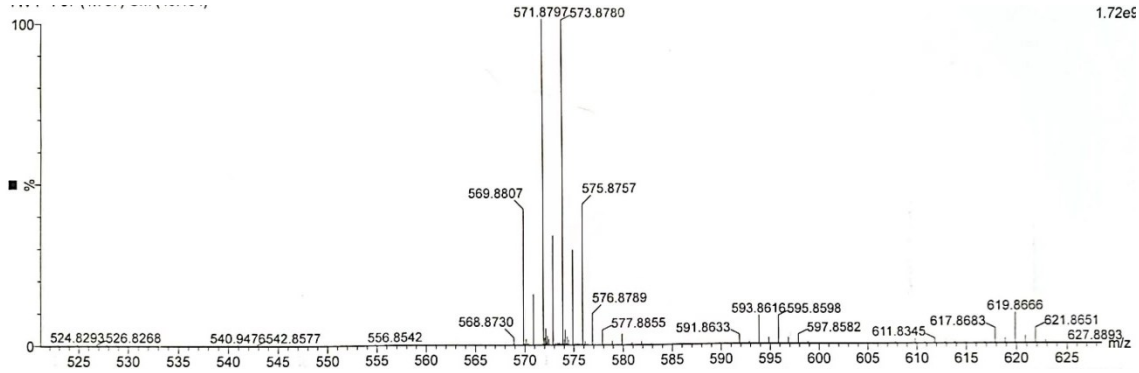

Figure S3. The HR-ESI-MS of **tris(4-bromo-2-methoxyphenyl)amine**.

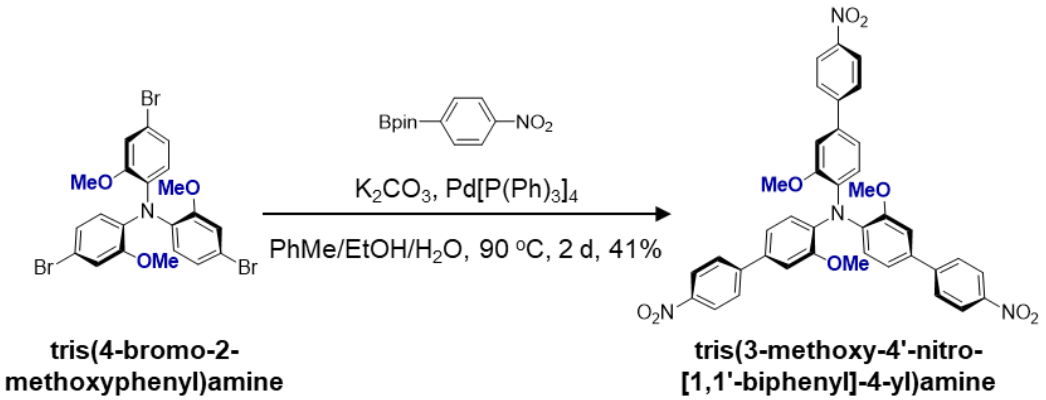

tris(4-bromo-2-methoxyphenyl)amine — **tris(3-methoxy-4'-nitro-[1,1'-biphenyl]-4-yl)amine**

Synthesis of tris(3-methoxy-4'-nitro-[1,1'-biphenyl]-4-yl)amine: To a solution of **tris(4-bromo-2-methoxyphenyl)amine** (3.00 g, 5.3 mmol) in Toluene/EtOH/H_2O (35 mL/5 mL/3 mL) was added $Pd[P(Ph)_3]_4$ (300 mg, 0.26 mmol), K_2CO_3 (2.0 g, 14.5 mmol), and 4,4,5,5-tetramethyl-2-(4-nitrophenyl)-1,3,2-dioxaborolane (6.60 g 26.5 mmol). Then, the mixture was stirred at 90 °C under a nitrogen atmosphere for 2 d. After cooling, the mixture was extracted with CH_2Cl_2 (3 × 50 mL) and washed by H_2O and brine, respectively. The organic layer was dried by anhydrous Na_2SO_4 and evaporated using a reduced pressure technique. The residue was subjected to a purification process via silica gel short column chromatography with *n*-hexane/CH_2Cl_2/EtOAc (20/0/1 to 20/10/2) to obtain **tris(3-methoxy-4'-nitro-[1,1'-biphenyl]-4-yl)amine** as a claybank solid in 41% yield. ^{1}H NMR (400 MHz, $CDCl_3$) δ 8.32 (d, J = 8.8 Hz, 6H), 7.78 (d, J = 8.9 Hz, 6H), 7.21 – 7.17 (m, 6H), 7.03 (d, J = 8.7 Hz, 3H), 3.74 (s, 9H). ^{13}C NMR (100 MHz, $CDCl_3$) δ 153.5, 147.3, 146.8, 137.8, 134.9, 127.34, 125.2, 124.2, 120.1, 111.7, 56.2. HRMS (ESI) *m/z* $[M + H]^+$ Calcd for $C_{39}H_{31}N_4O_9$ 699.2086, found 699.2026.

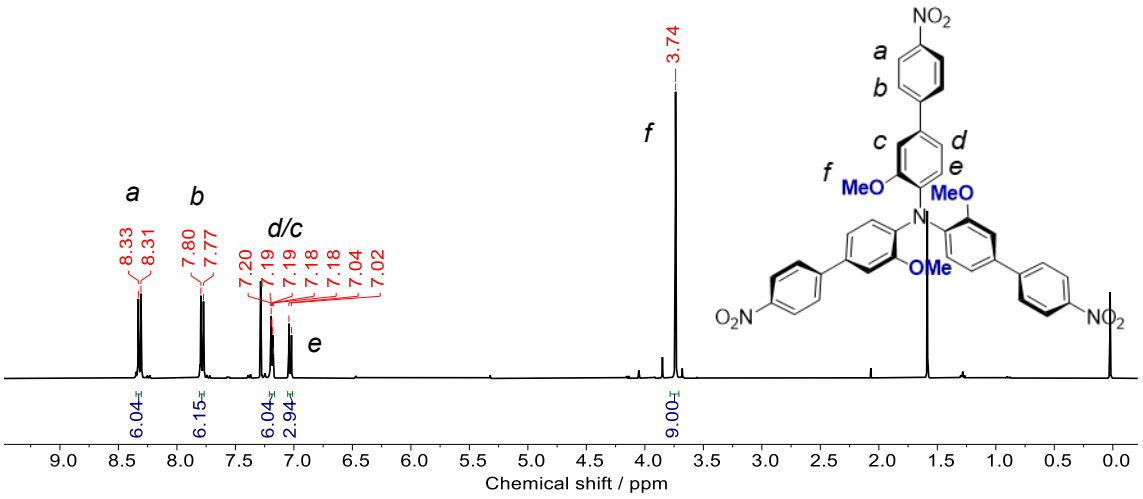

Figure S4. ^{1}H NMR spectrum of **tris(3-methoxy-4'-nitro-[1,1'-biphenyl]-4-yl)amine** (400 MHz, $CDCl_3$, 298 K).

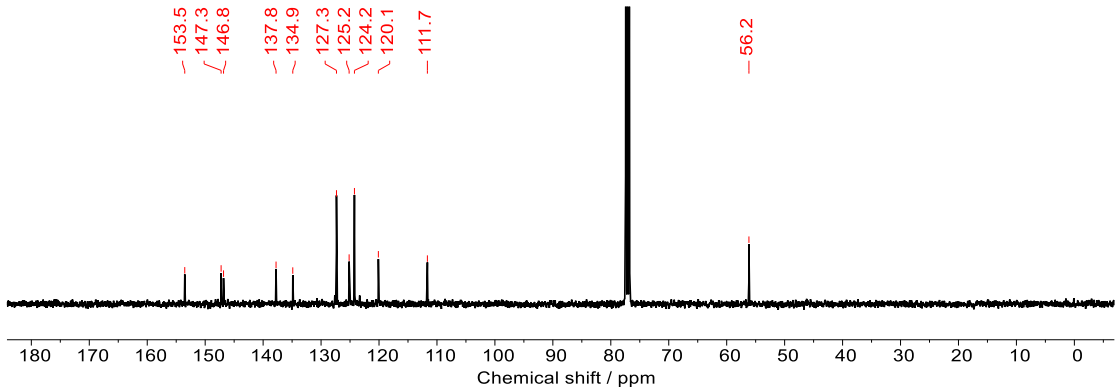

Figure S5. ^{13}C NMR spectrum of **tris(3-methoxy-4'-nitro-[1,1'-biphenyl]-4-yl)amine** (101 MHz, $CDCl_3$, 298 K).

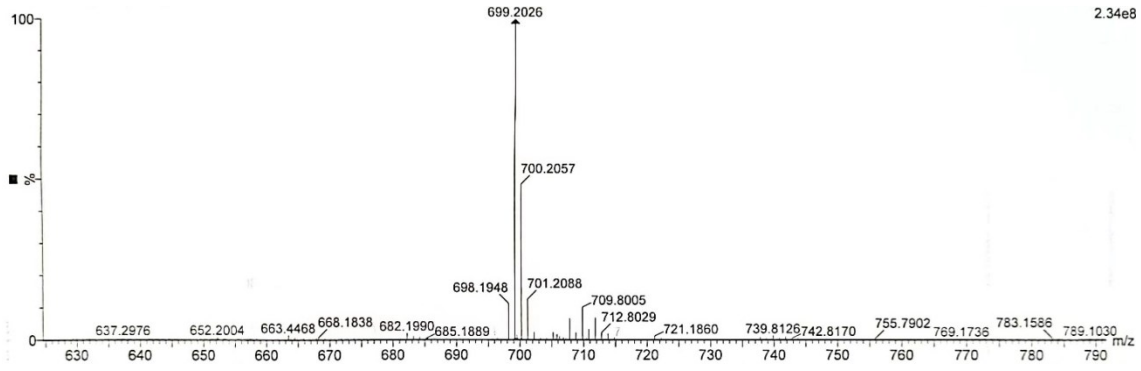

Figure S6. The HR-ESI-MS of **tris(3-methoxy-4'-nitro-[1,1'-biphenyl]-4-yl)amine**.

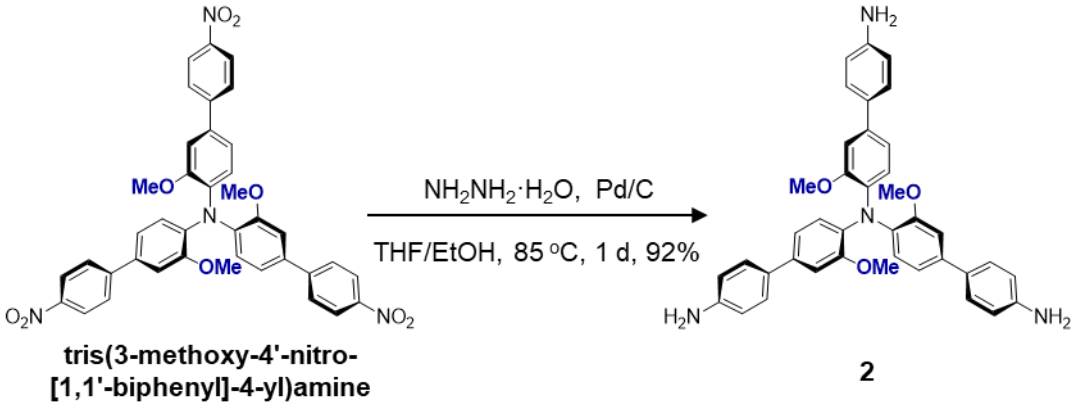

tris(3-methoxy-4'-nitro-[1,1'-biphenyl]-4-yl)amine

2

Synthesis of 2: To a stirred solution of **tris(3-methoxy-4'-nitro-[1,1'-biphenyl]-4-yl)amine** (600 mg) in EtOH/THF (50 mL/30 mL) was added 300 mg Pd/C. Then the solution was refluxed in a nitrogen atmosphere for 1 d. After cooling to RT, the mixture was filtrated, and an off-white solid of **2** was obtained in a 92% yield by evaporating the solvent under reduced pressure. ^{1}H NMR (396 MHz, DMSO-d_6) δ 7.32 (d, J = 8.6 Hz, 6H), 7.06 (d, J = 2.1 Hz, 3H), 6.98 (dd, J = 8.3, 2.1 Hz, 3H), 6.68 (d, J = 8.2 Hz, 3H), 6.61 – 6.57 (m, 6H), 5.12 (s, 6H), 3.57 (s, 9H). ^{13}C NMR (101 MHz, DMSO-d_6) δ 153.7, 148.4, 136.8, 136.0, 127.9, 127.3, 125.2, 118.3, 114.6, 111.6, 56.6. HRMS (ESI) m/z $[M + H]^+$ Calcd for $C_{39}H_{37}N_4O_3$ 609.2860, found 609.2819.

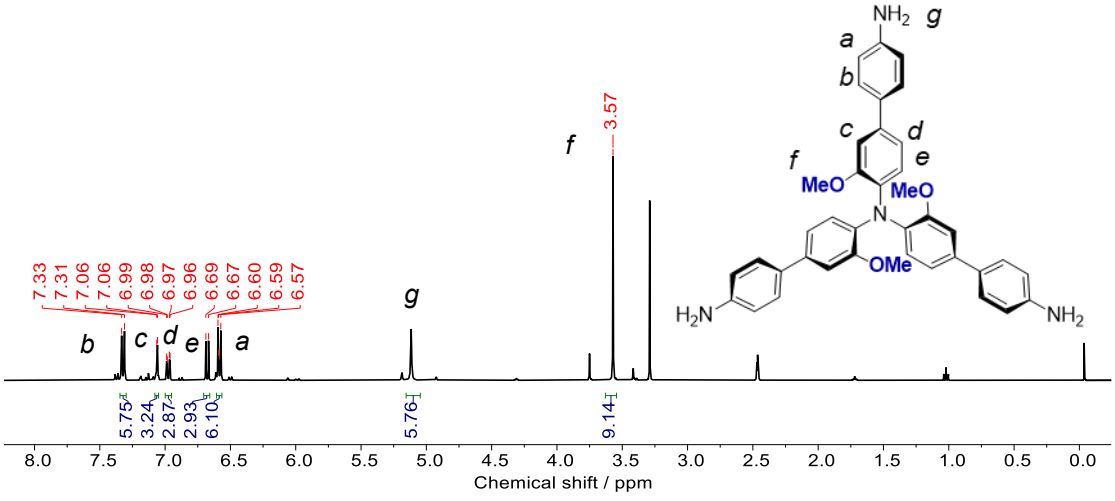

Figure S7. ^{1}H NMR spectrum of **2** (400 MHz, DMSO-d_6, 298 K).

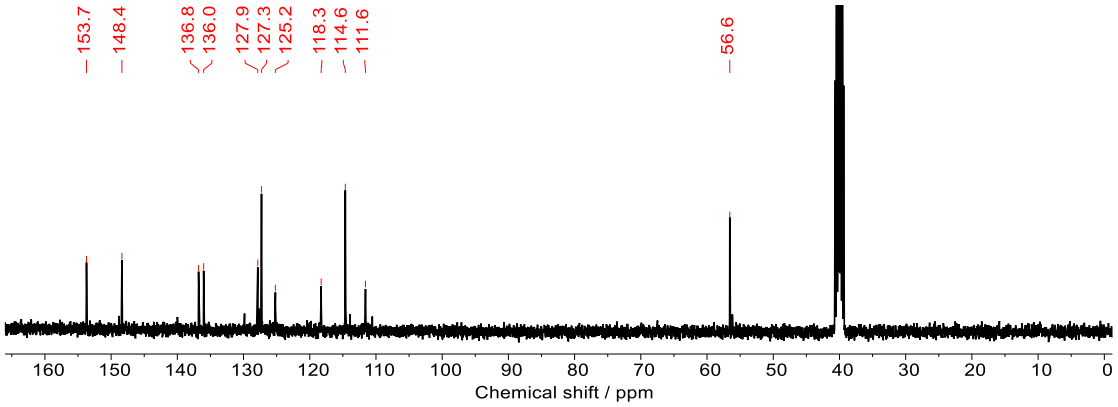

Figure S8. ^{13}C NMR spectrum of **2** (101 MHz, DMSO-d_6, 298 K).

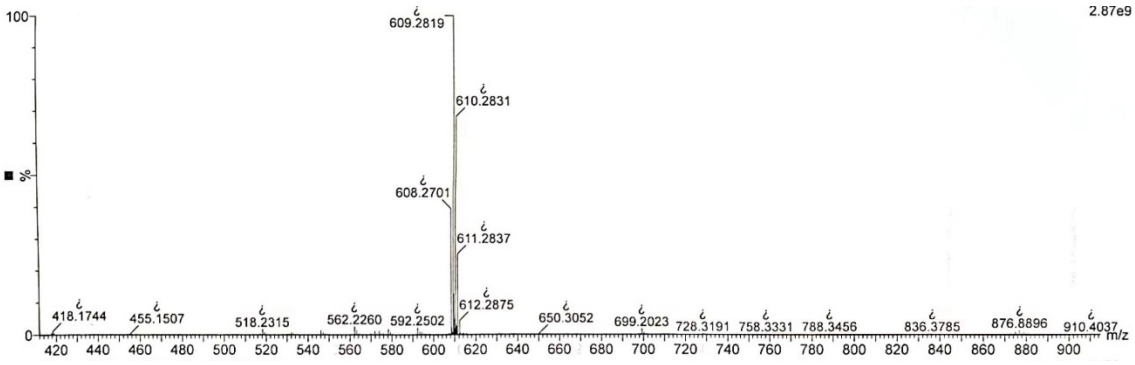

Figure S9. The HR-ESI-MS of **2**.

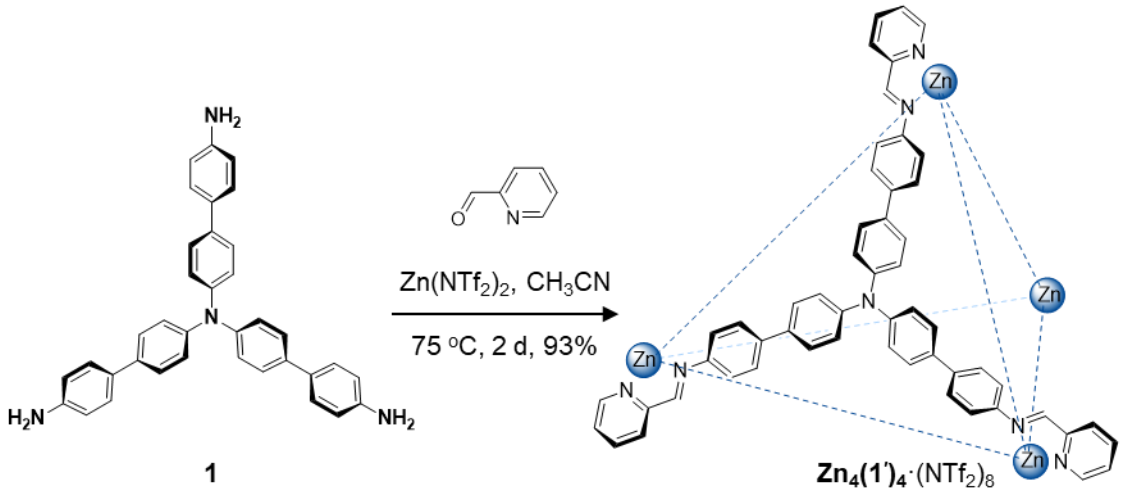

Synthesis of $Zn_4(1')_4\cdot(NTf_2)_8$: Zinc(II) Bis(trifluoromethanesulfonyl)imide (6.3 mg, 0.01 mmol), **1** (6.1 mg, 0.01 mmol), and 2-formylpyridine (16 μL, 0.17 mmol) were dissolved in MeCN (2.5 mL). The reaction mixture was rigorously stirred under a nitrogen atmosphere at 75 °C for 2 d. The mixture

was filtered and Et_2O (35 mL) was added. The black precipitate was thoroughly collected by centrifugation and washed with excess Et_2O several times to give $\mathbf{Zn_4(1')_4}\cdot(NTf_2)_8$ in a 93% yield. ^1H NMR (500 MHz, CD_3CN) δ 8.71 (s, 12H), 8.42 (td, J = 7.8, 1.5 Hz, 12H), 8.24 (d, J = 7.8 Hz, 12H), 7.82 (ddd, J = 7.8, 5.1, 1.2 Hz, 12H), 7.73 (d, J = 5.0 Hz, 12H), 7.55 (d, J = 8.7 Hz, 24H), 7.45 (d, J = 8.7 Hz, 24H), 7.15 (d, J = 8.7 Hz, 24H), 6.53 (d, J = 8.6 Hz, 24H). ^{19}F NMR (471 MHz, CD_3CN) δ -79.92. HRMS (ESI) *m/z* $[\mathbf{Zn_4(2')_4}\cdot(NTf_2)_2]^{6+}$ Calcd for $(C_{216}H_{156}N_{28}Zn_4 + C_4F_{12}N_2O_8S_4)^{6+}$ 660.8090, found 660.8120; *m/z* $[\mathbf{Zn_4(2')_4}\cdot(NTf_2)_3]^{5+}$ Calcd for $(C_{216}H_{156}N_{28}Zn_4 + C_6F_{18}N_3O_{12}S_6)^{5+}$ 848.9545, found 848.9585.

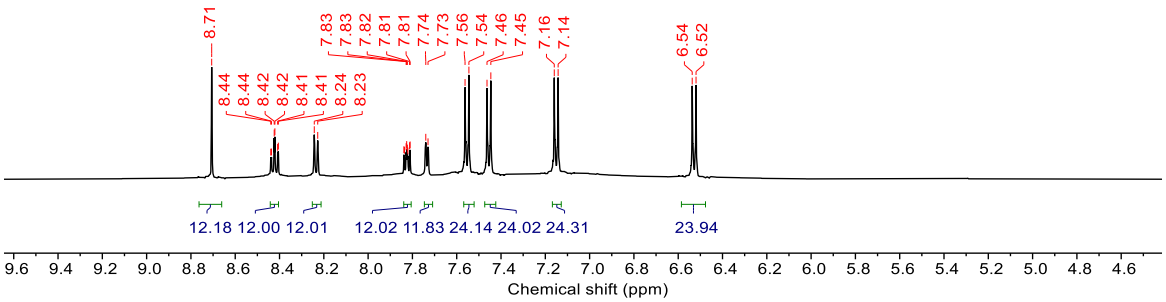

Figure S10. ^1H NMR spectrum of $\mathbf{Zn_4(1')_4}\cdot(NTf_2)_8$ (500 MHz, CD_3CN, 298 K).

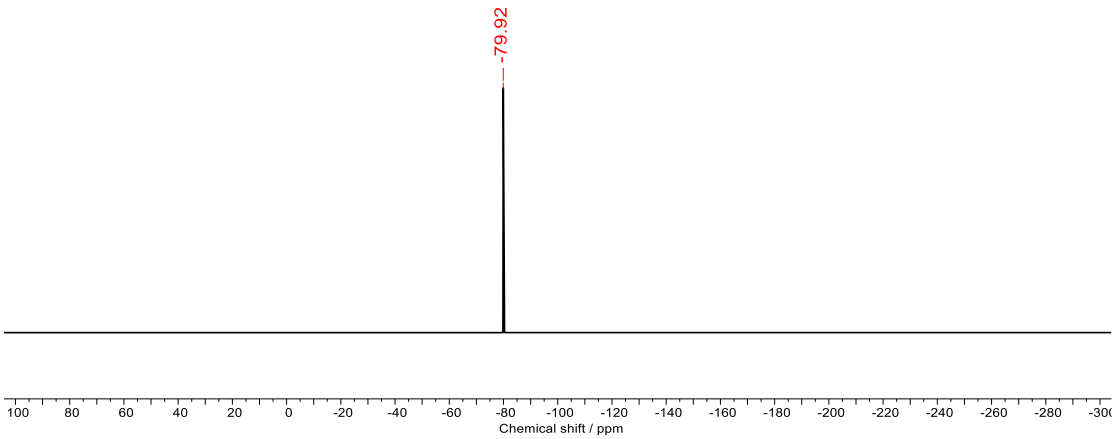

Figure S11. ^{19}F NMR spectrum of $\mathbf{Zn_4(1')_4}\cdot(NTf_2)_8$ (471 MHz, CD_3CN, 298 K).

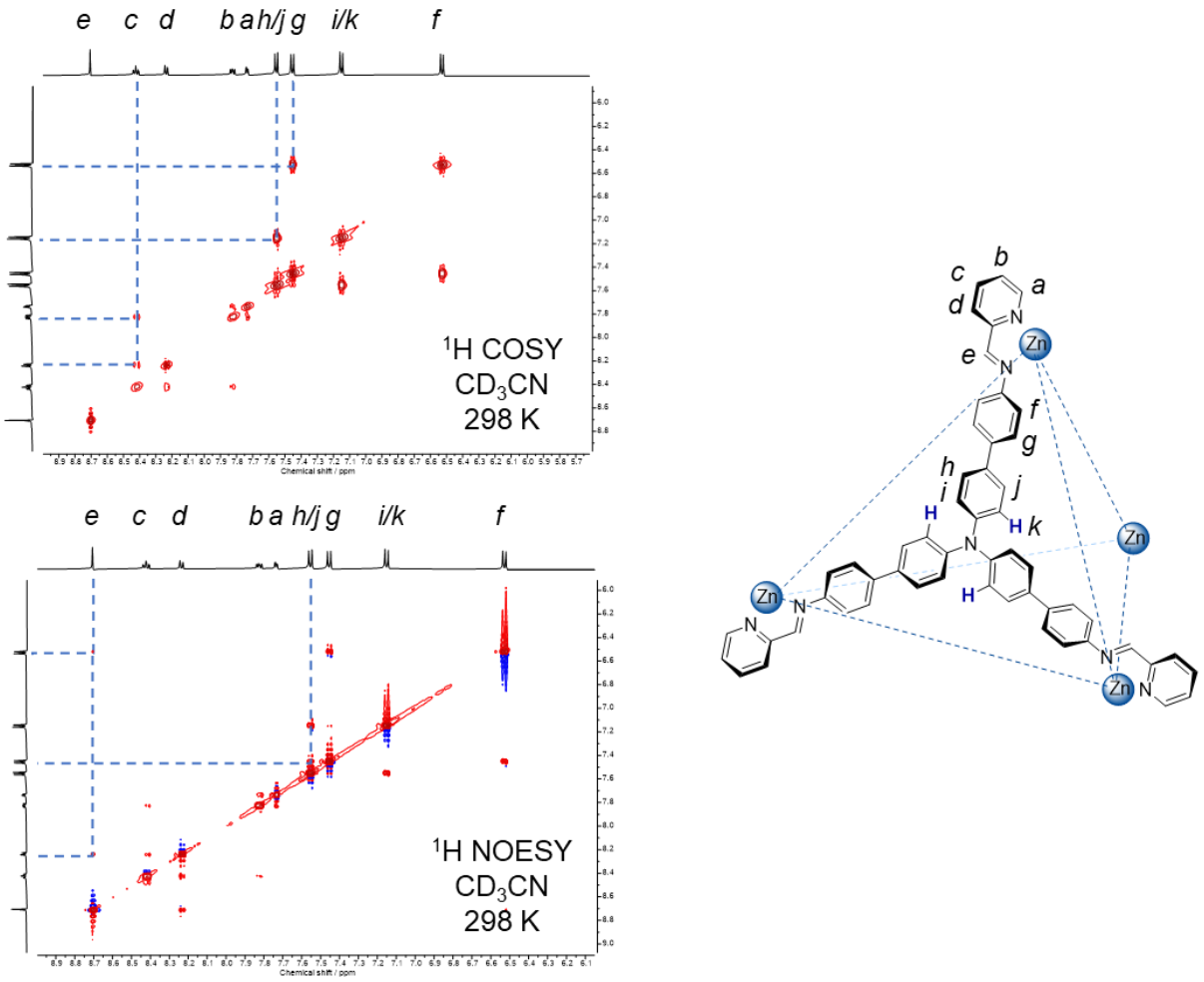

Figure S12. ^{1}H COSY and NOESY spectra of $\mathbf{Zn_4(1')_4}\cdot(NTf_2)_8$ monitored in CD_3CN (500 MHz, 298 K).

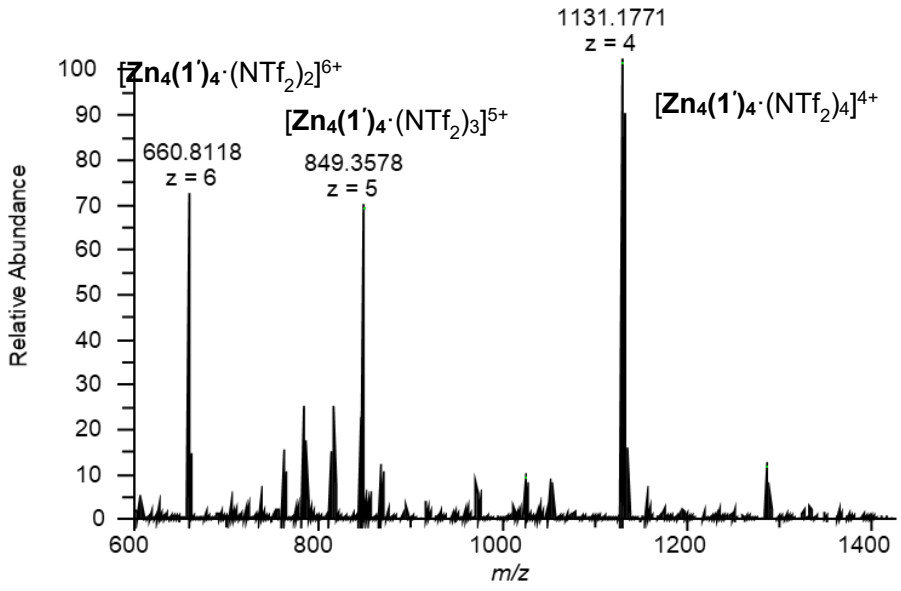

Figure S13. The HR-ESI-MS of $\mathbf{Zn_4(1')_4}\cdot(NTf_2)_8$.

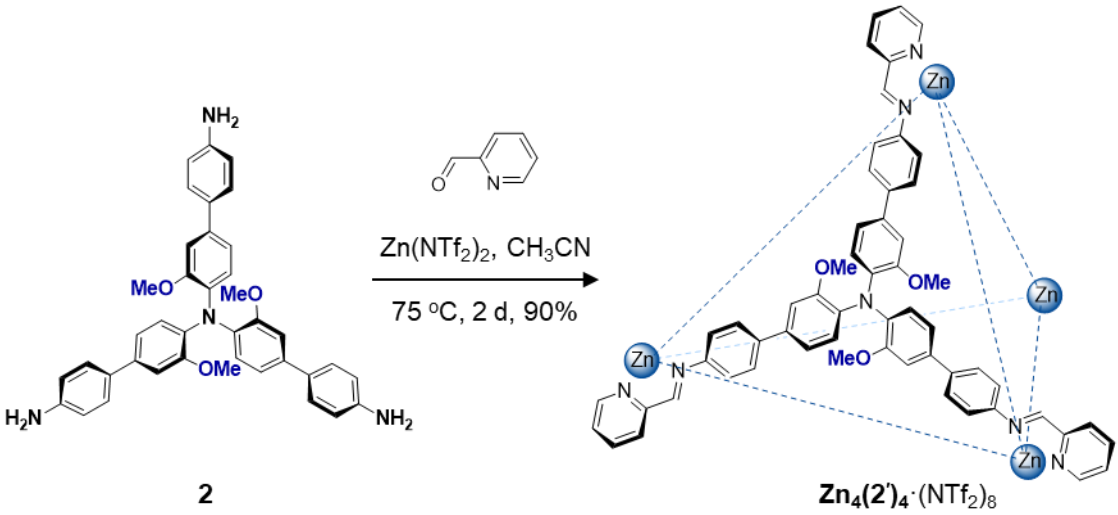

Synthesis of $Zn_4(2')_4\cdot(NTf_2)_8$: Zinc(II) Bis(trifluoromethanesulfonyl)imide (6.3 mg, 0.01 mmol), **2** (5.2 mg, 0.01 mmol), and 2-formylpyridine (16 μL, 0.17 mmol) were dissolved in MeCN (2.5 mL). The reaction mixture was vigorously stirred under a nitrogen atmosphere at 75 °C for 2 d. The mixture was filtered and Et_2O (25 mL) was added. The black precipitate was thoroughly collected by centrifugation and washed with excess Et_2O several times to give $\mathbf{Zn_4(2')_4}\cdot(NTf_2)_8$ in a 90% yield. ^{1}H NMR (400 MHz, CD_3CN) δ 8.75 (s, 12H), 8.51 – 8.46 (m, 12H), 8.29 (d, J = 8.1 Hz, 12H), 7.91 – 7.81 (m, 24H), 7.58 (d, J = 8.4 Hz, 24H), 7.29 – 7.16 (m, 24H), 6.84 (d, J = 8.4 Hz, 12H), 6.58 (d, J = 8.2 Hz, 24H), 3.70 (s, 36H). ^{19}F NMR (471 MHz, CD_3CN) δ -79.98. HRMS (ESI) *m/z* $[\mathbf{Zn_4(1')_4}\cdot(NTf_2)_2]^{6+}$ Calcd for $(C_{228}H_{180}N_{28}O_{12}Zn_4 + C_4F_{12}N_2O_8S_4)^{6+}$ 720.8305, found 720.8315; *m/z* $[\mathbf{Zn_4(1')_4}\cdot(NTf_2)_3]^{5+}$ Calcd for $(C_{228}H_{180}N_{28}O_{12}Zn_4 + C_6F_{18}N_3O_{12}S_6)^{5+}$ 921.1799, found 921.1813.

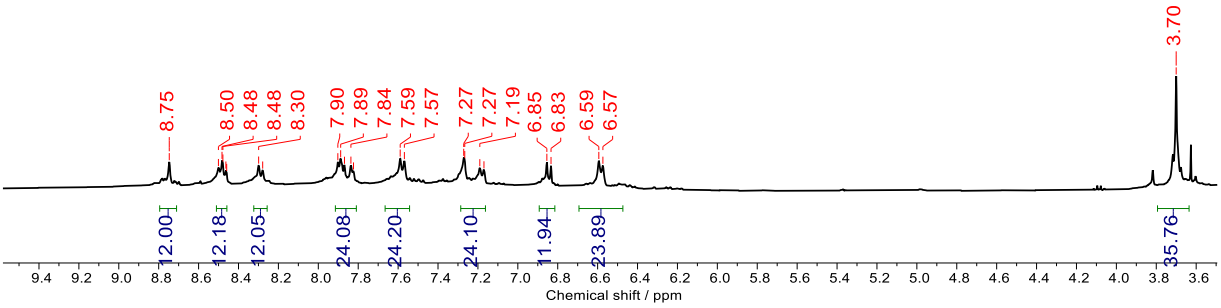

Figure S14. ^{1}H NMR spectrum of $\mathbf{Zn_4(2')_4}\cdot(NTf_2)_8$ (400 MHz, CD_3CN, 298 K).

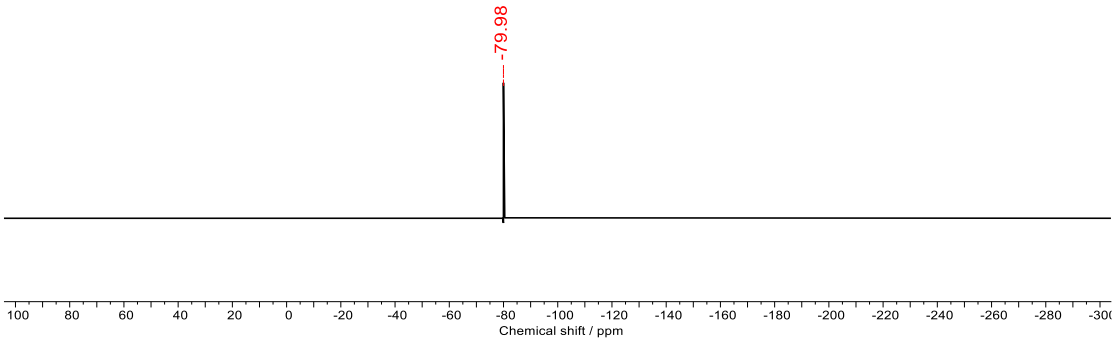

Figure S15. ^{19}F NMR spectrum of **Zn$_4$(2′)$_4$**·(NTf$_2$)$_8$ (471 MHz, CD$_3$CN, 298 K).

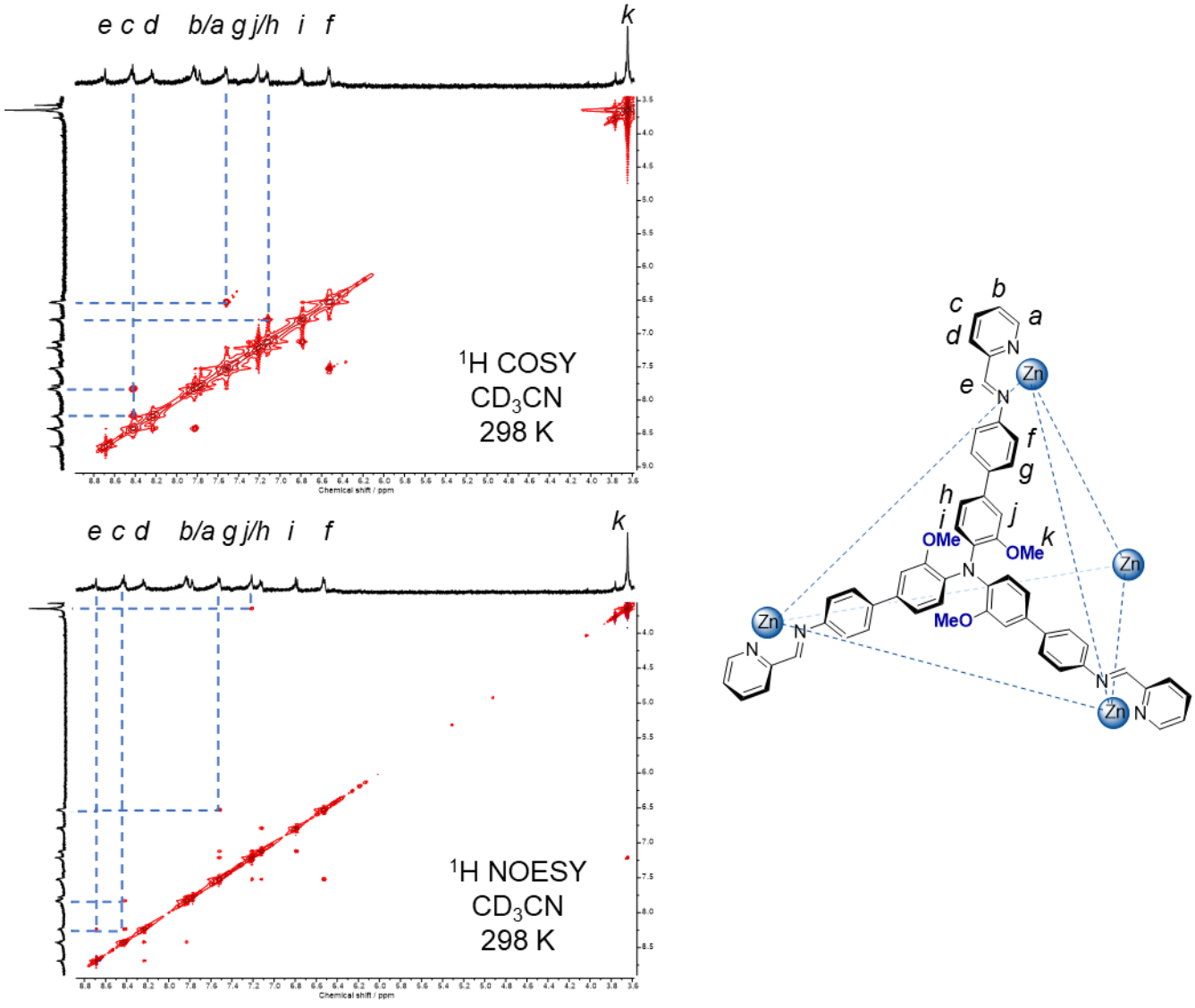

Figure S16. ^{1}H COSY and NOESY spectra of **Zn$_4$(2′)$_4$**·(NTf$_2$)$_8$ monitored in CD$_3$CN (500 MHz, 298 K).

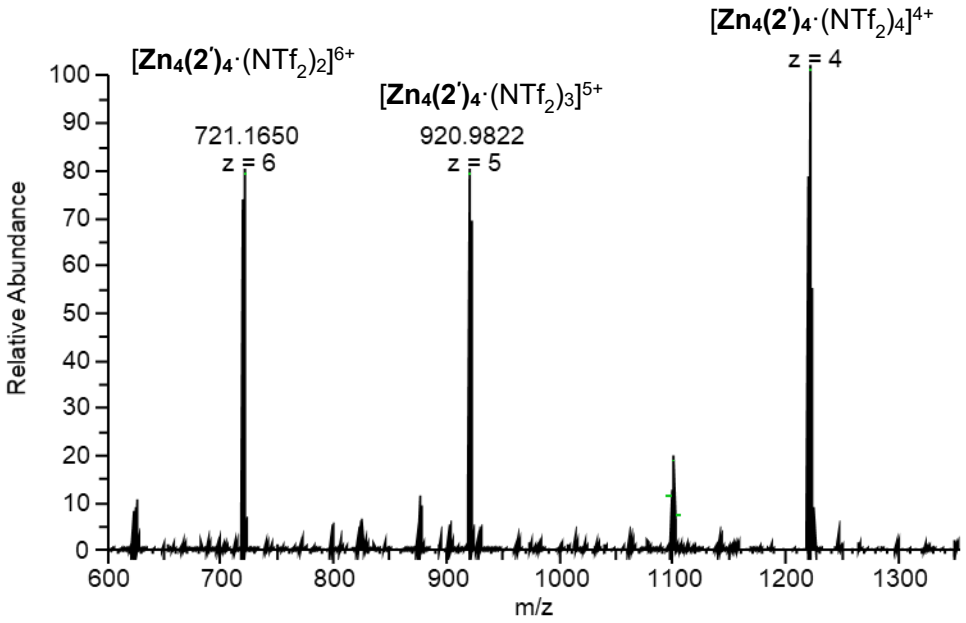

Figure S17. The HR-ESI-MS of $\mathbf{Zn_4(2')_4}\cdot(NTf_2)_8$.

Computational Analysis

All of the calculations were performed using Gaussian 16 Revision C.01 software.[1] Specifically, the structures of MOC and host-guest complex were optimized at DFT-D_3 b3lyp/3-21g level. The IGM analysis was realized by the Multiwfn.[2] The available cavity volumes of MOCs were performed using Molovol,[3] and all parameters were set at their default values, except the small probe radius (3 Å).

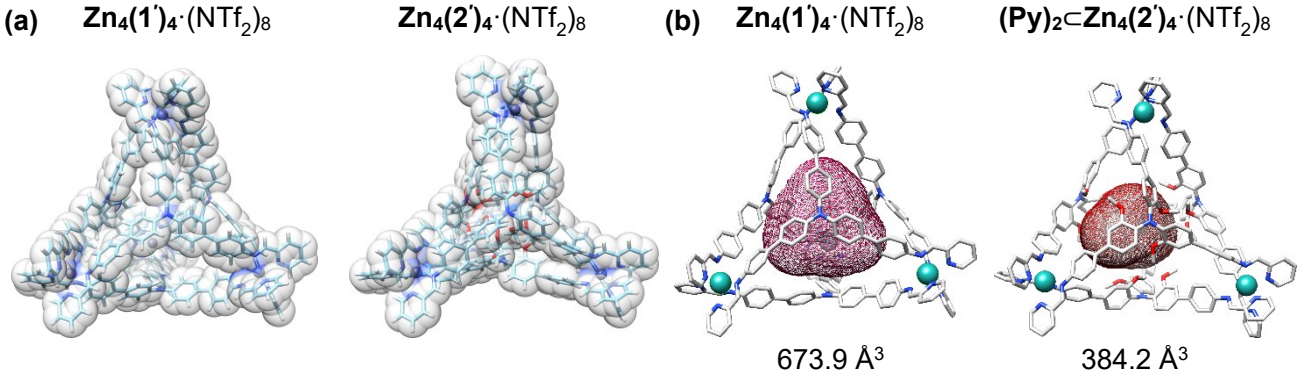

Figure S18. (a) DFT-optimized structures of $\mathbf{Zn_4(1')_4}\cdot(NTf_2)_8$ and $\mathbf{Zn_4(2')_4}\cdot(NTf_2)_8$. (b) Calculated cavity volumes of $\mathbf{Zn_4(1')_4}\cdot(NTf_2)_8$ and $\mathbf{(Py)_2\subset Zn_4(2')_4}\cdot(NTf_2)_8$.

In our calculation of the cavity volume for **(Py)$_2$⊂Zn$_4$(2′)$_4$**·(NTf$_2$)$_8$, the perylene guests were omitted to evaluate the available space. In the pristine (guest-free) state, multiple weak interactions among adjacent methoxy (–OMe) groups cause the framework to collapse inward, resulting in an intrinsically small and poorly defined cavity. Upon encapsulation of the perylene dimer, the host framework undergoes a self-adaptive structural adjustment via an induced-fit mechanism. This expansion creates a more commensurate internal space (ca. 384.2 Å^3) defined by the OMe-lined periphery. Notably, the calculated volume of the dimerized perylene (489.1 Å^3) exceeds the formally defined internal cavity volume (384.2 Å^3). This discrepancy indicates that the guests are not entirely "sequestered" within a closed cavity; instead, they protrude beyond the OMe-mediated boundary, which is confirmed by our simulated structures (Figure 3c, S18). Such a phenomenon is consistent with the open and irregular architecture of the cage, as opposed to a strictly confined, closed-surface container. This structural flexibility allows the host to accommodate guests that technically exceed the traditional volumetric limits. For such open and irregular cavities, precise volume determination is inherently ambiguous. To visualize the intrinsic internal cavity, peripheral regions outside the OMe-lined boundary were intentionally excluded from the cavity calculation, leading to an apparent internal volume smaller than that of the encapsulated perylene dimer. Consequently, the present system does not strictly conform to the conventional Rebek limit (~55%), which is expected for rigid, regular cavities.[4,5]

We attribute this selective behavior to a synergistic effect of size-matching and specific non-covalent interactions. Specifically, the introduction of methoxy (-OMe) groups onto the TPA moieties is crucial for modulating the cavity's microenvironment, facilitating strong C−H···O and C−H···π interactions with the guest. Perylene exhibits a strong propensity to dimerize in solution; this dimeric form possesses the ideal geometry and volume to perfectly complement the host cavity, leading to stable encapsulation. In contrast, while other smaller molecules might also undergo dimerization, their resulting dimers lack the necessary geometric complementarity to be effectively stabilized by the cage's internal framework. Admittedly, the rational design of guest-specific molecular containers remains a significant challenge in supramolecular chemistry, and we intend to explore the underlying predictive principles more deeply in our future research.

Guest Molecules Used for Host-Guest Recognition

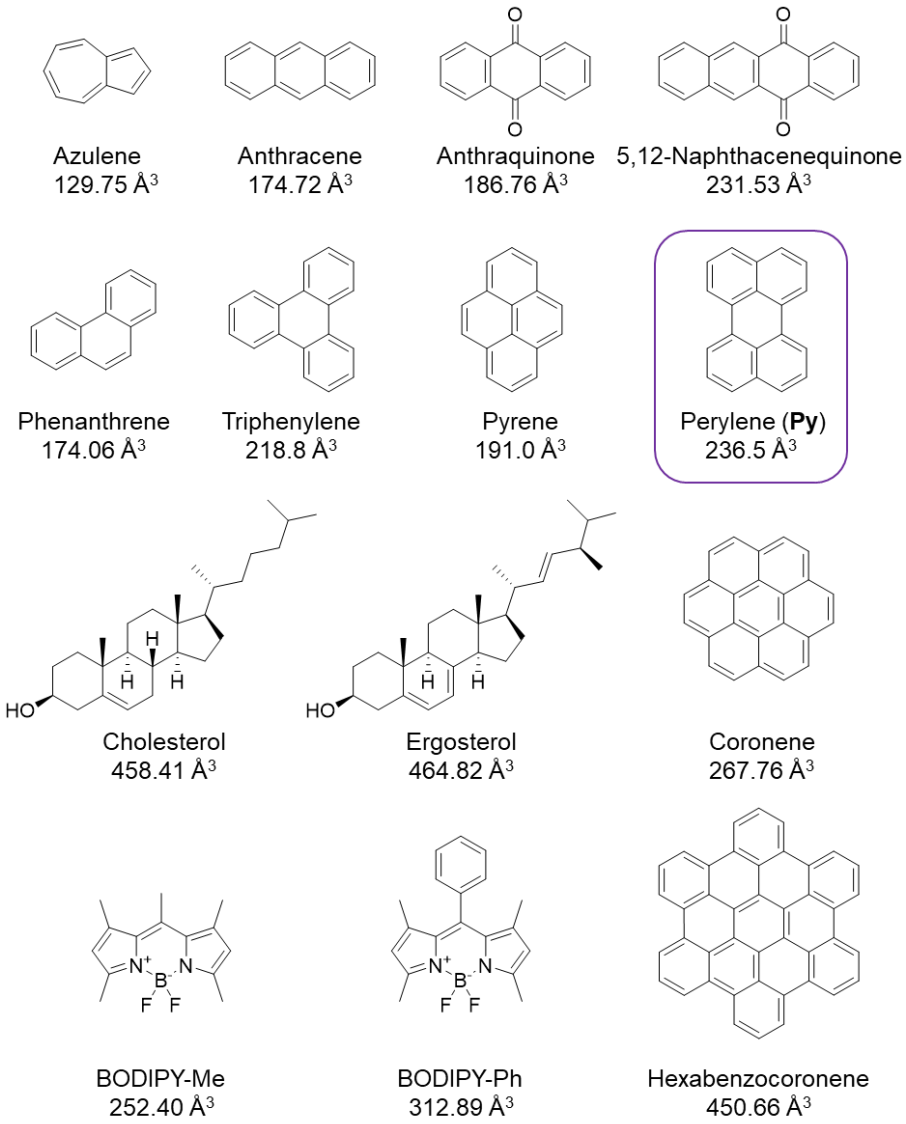

Figure S19. Guest molecules and their calculated molecular volumes used for host–guest recognition by MOCs.

Typically, an NMR tube was charged with 6 mg of MOCs, followed by 0.5 mL of CD_3CN to afford a clear solution. Approximately 10 equivalents of guest molecules were then added, the tube was capped, and the mixture was heated at 50 °C for 24 h. The sample was subsequently analysed by ^1H NMR to evaluate host–guest behaviour in situ. After NMR test, the solution was diluted to perform HR-ESI-MS for monitoring the recognition behaviour. Both experiments indicated that only $\mathbf{Zn_4(2')_4}\cdot(NTf_2)_8$ can recognize perylene (**Py**) with a host-guest ratio of 1:2.

Fluorometric titration experiments were performed by tracking the fluorescence quenching of **Py** with a range of equivalents of **Zn$_4$(2′)$_4$**·(NTf$_2$)$_8$. A plot of fluorescent intensity versus **Zn$_4$(2′)$_4$**·(NTf$_2$)$_8$ concentration was fitted with a nonlinear least-squares fitting equation for 1:1 binding model to calculate the binding constant K_a using OriginPro 9.0 software.[6]

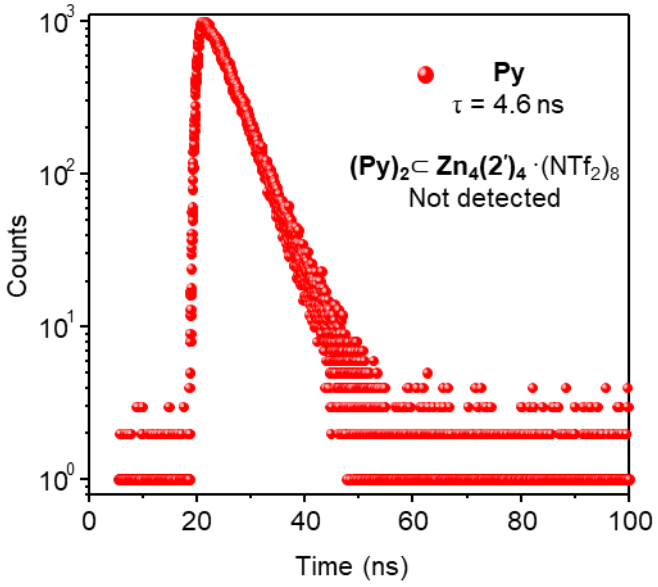

Figure S20. Fluorescent decay curves of **Py** and **(Py)$_2$⊂Zn$_4$(2′)$_4$**·(NTf$_2$)$_8$ (2×10^{-5} M in MeCN).

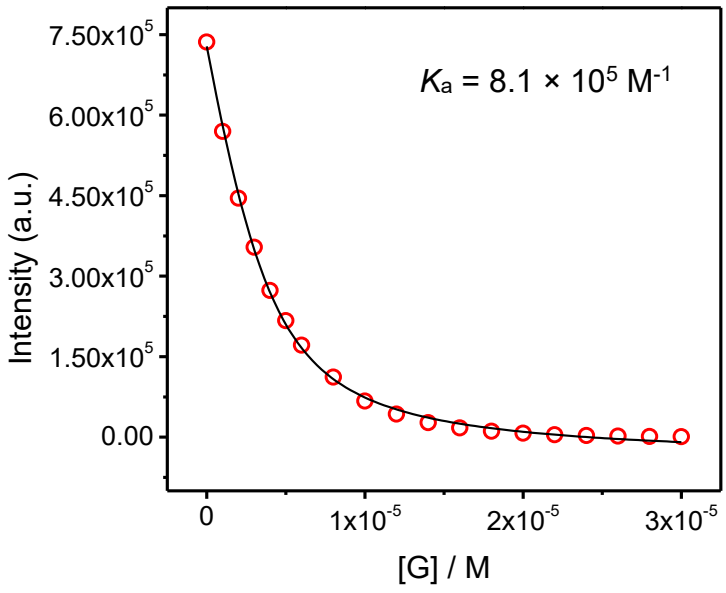

Figure S21. The calibrated titration curve at λ_{em} = 441 nm and fit according to a 1:1 binding model between **Py** dimers and **Zn$_4$(2′)$_4$**·(NTf$_2$)$_8$, where **Py** molecules are dimerized and encapsulated into the cavity simultaneously.

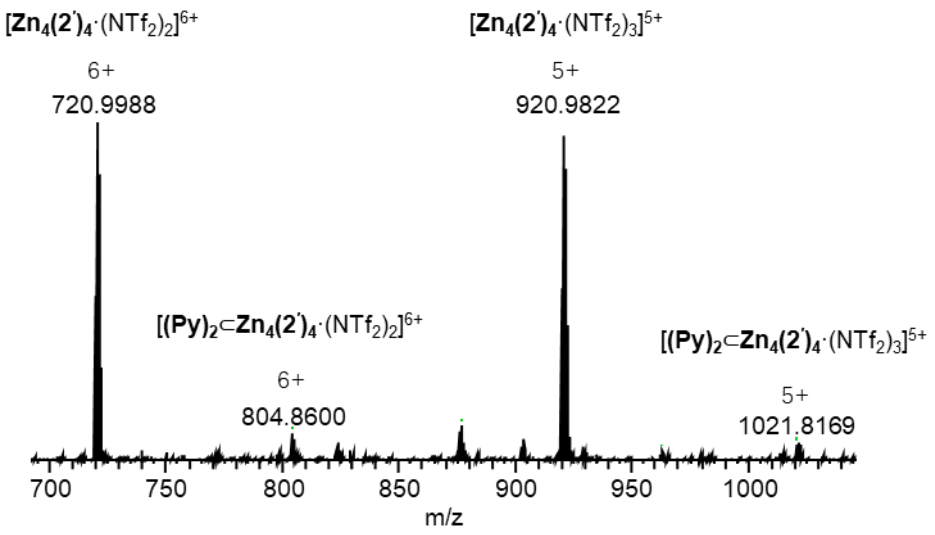

Figure S22. HR-ESI-MS of $\mathbf{Zn_4(2')_4}\cdot(NTf_2)_8$ with access addition of **Py**.

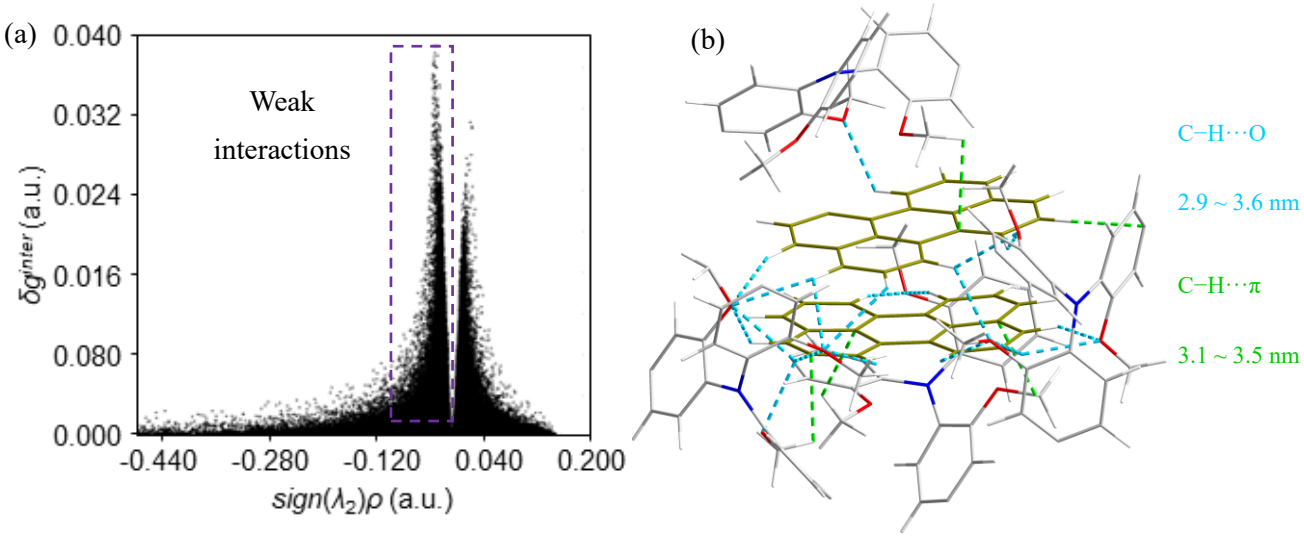

Figure S23. (a) IGM analysis of the weak interactions between $\mathbf{Zn_4(2')_4}\cdot(NTf_2)_8$ and perylene dimers. (b) C–H···O (blue dash line) and C–H···π (green dash line) interactions between perylene dimers and TPA moieties from $\mathbf{Zn_4(2')_4}\cdot(NTf_2)_8$.

Assembly of NPs

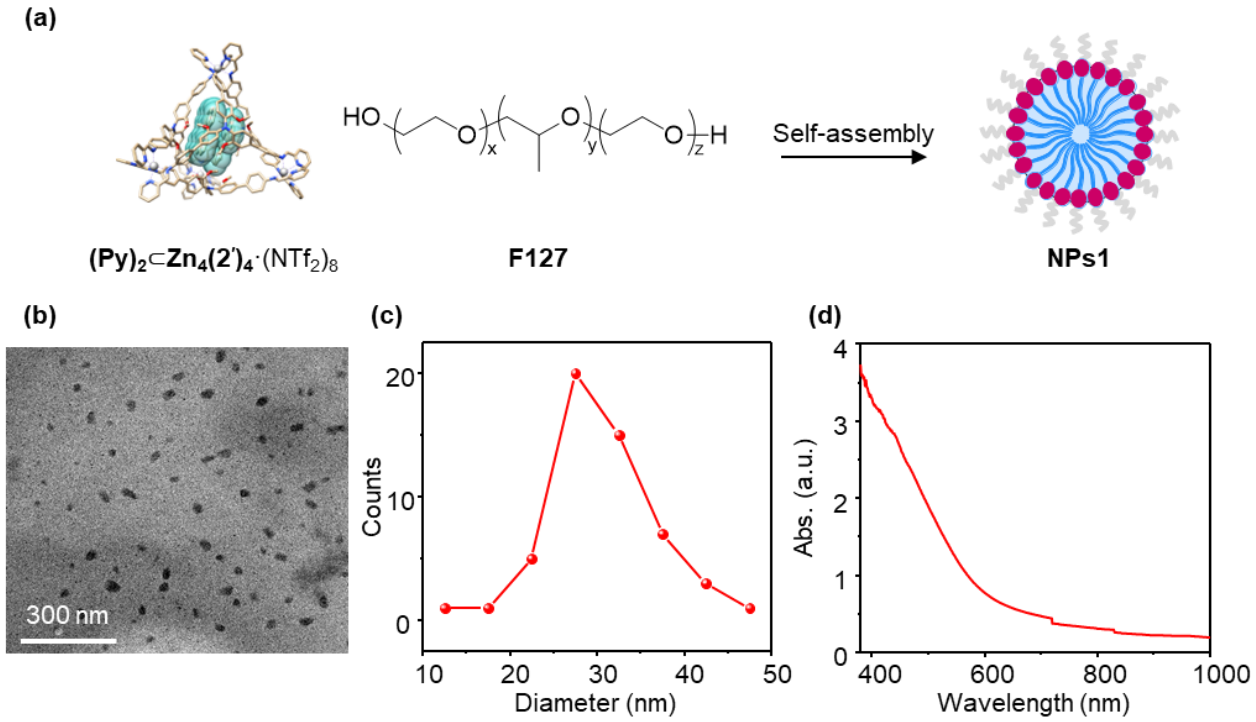

Figure S24. (a) Schematic depiction for **NPs1** preparation using **(Py)$_2$⊂Zn$_4$(2′)$_4$**·(NTf$_2$)$_8$ and **F127**. TEM images (b) of **NPs1** and their size distribution analysis (c). (d) Absorbance spectra of **NPs1** (0.1 mg/mL).

Preparation of **NPs1**: To a solution of freshly prepared cage **Zn$_4$(2′)$_4$**·(NTf$_2$)$_8$ (10 mg) in MeCN (1.5 mL), excess perylene (ca. 5 mg) was added. The mixture was heated at 50 °C for 24 h. After cooling to RT, the solution was filtered. The resulting filtrate was added dropwise into diethyl ether (Et$_2$O, 10 mL) to precipitate the host-guest complex **(Py)$_2$⊂Zn$_4$(2′)$_4$**·(NTf$_2$)$_8$, which was obtained in 95% yield. Subsequently, **(Py)$_2$⊂Zn$_4$(2′)$_4$**·(NTf$_2$)$_8$ (0.1 mg) and **F127** (2.5 mg) were dissolved in deionized water (1 mL). The mixture was stirred for 30 min at RT, resulting in the formation of the complex nanoparticles (**NPs1**).

Preparation of **NPs2**: **Zn$_4$(2′)$_4$**·(NTf$_2$)$_8$ (0.1 mg) and F127 (2.5 mg) were dissolved in deionized water (1 mL). The mixture was stirred for 30 min at RT, resulting in the formation of the cage nanoparticles (**NPs2**).

Preparation of **NPs3**: Perylene (0.1 mg) and F127 (2.5 mg) were dissolved in deionized water (1 mL). The mixture was stirred for 30 min at RT, resulting in the formation of the cage nanoparticles (**NPs3**).

Antibacterial Experiments

For confocal laser scanning microscopy imaging: 100 μg/ml **NPs** were treated with bacteria in presence of 20 um DCFDA solution without or with light irradiation. Aftertreatment, bacteria were pelleted and resuspended in PBS for imaging using 100 oil objectives.

Light-irradiation antibacterial test: Prepare 0.1mg/ml **NPs** solution in 10 ml PBS, sonication to well-dispersed solution, add 100 μL 10^9 CFU/ml bacteria suspension, mix well, then irradiate using 300 W Xenon light for 30 min, 1 h and 2 h respectively, take 50 μL bacterial suspension and spread on 90 mm petri dish agar and incubate overnight at 37 Celsius degree to grow.

In Vitro ROS Detection (Figure 4a): DCFH-DA was utilized as a fluorogenic probe to quantify ROS generation in solution. The probe is first chemically hydrolyzed by NaOH to remove the acetyl groups, converting the non-fluorescent DCFH-DA into DCFH. Upon the generaion of ROS by light irradiation, DCFH undergoes oxidation to form DCF, a highly fluorescent species that serves as the indicator for ROS levels.

Intracellular ROS Detection: A parallel mechanism occurs within the cellular environment. Once internalized, the cell-permeable DCFH-DA is hydrolyzed by endogenous intracellular esterases into non-fluorescent DCFH. This intermediate is subsequently oxidized by intracellularly generated ROS to yield fluorescent DCF, allowing for the direct visualization of oxidative stress via fluorescence microscopy.

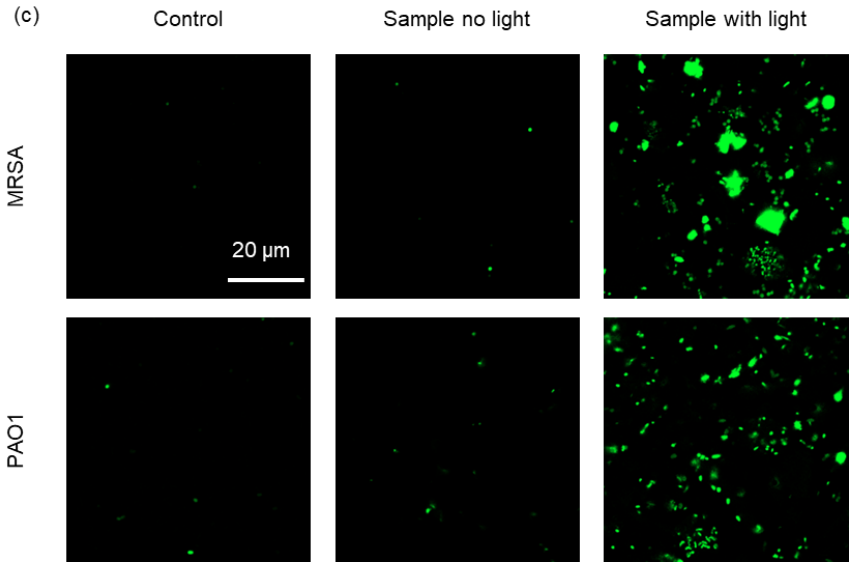

Figure S25. Intracellular ROS generation by **NPs** (0.1 mg/mL, H_2O) under white light irradiation.

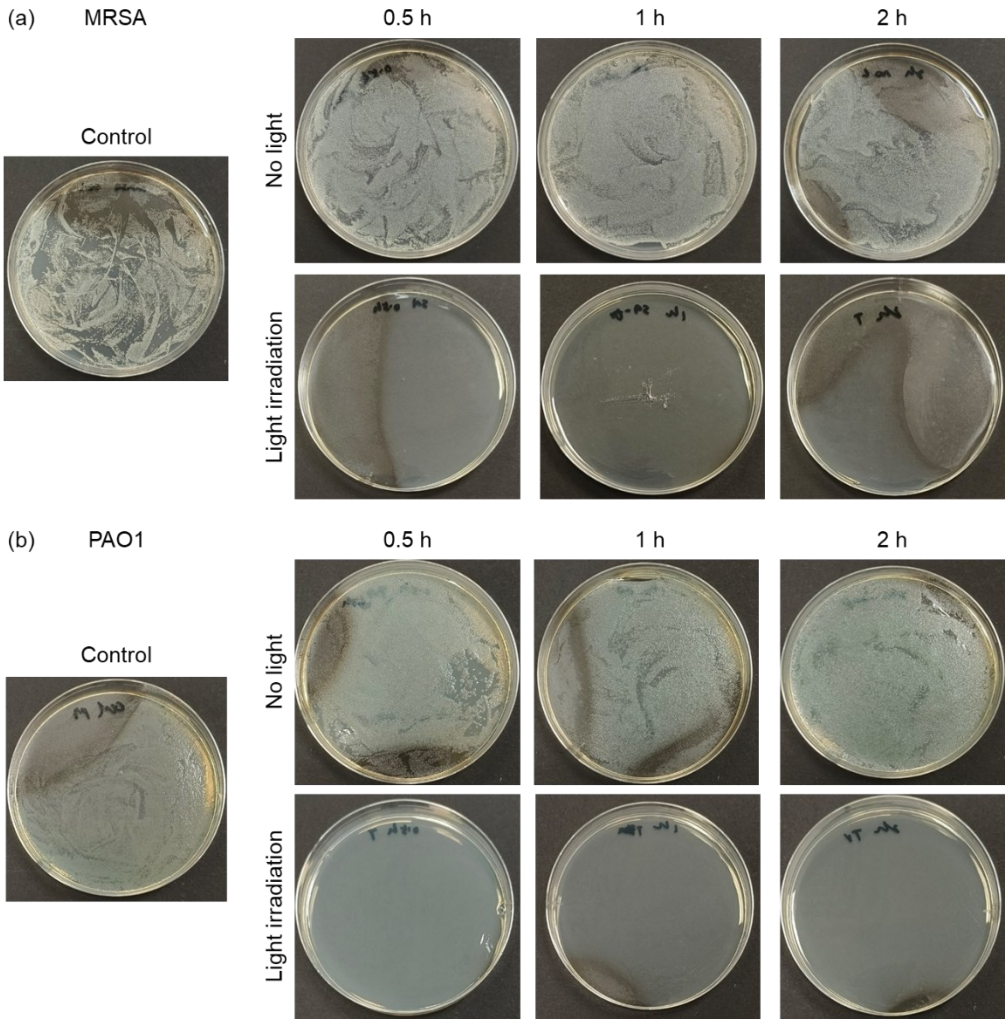

Figure S26. Antibacterial experiments of **NPs** towards MRSA and PAO1 (1.47×10^7 CFU/mL), where agar plates were inoculated with MRSA or PAO1 strains, respectively.

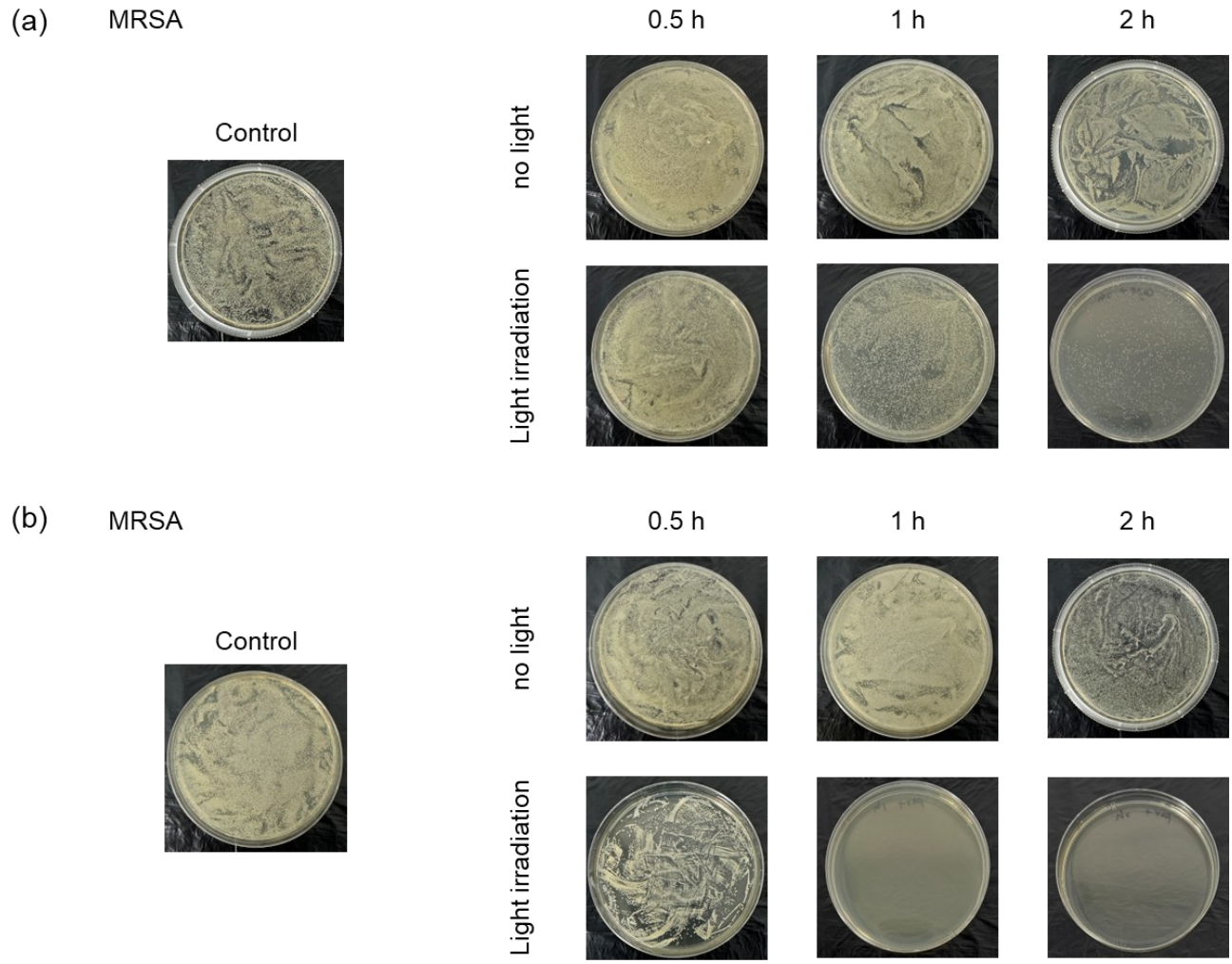

Figure S27. Antibacterial experiments of $\mathbf{Zn_4(2')_4}\cdot(NTf_2)_8$ **NPs2** (a) and perylene **NPs3 (b)** towards MRSA (1.47 × 107 CFU/mL), where agar plates were inoculated with MRSA strains.

References

[1] Gaussian 09, Revision D.01, M. J. Frisch, G. W. Trucks, H. B. Schlegel, G. E. Scuseria, M. A. Robb, J. R. Cheeseman, G. Scalmani, V. Barone, B. Mennucci, G. A. Petersson, H. Nakatsuji, M. Caricato, X. Li, H. P. Hratchian, A. F. Izmaylov, J. Bloino, G. Zheng, J. L. Sonnenberg, M. Hada, M. Ehara, K. Toyota, R. Fukuda, J. Hasegawa, M. Ishida, T. Nakajima, Y. Honda, O. Kitao, H. Nakai, T. Vreven, J. A. Montgomery, Jr., J. E. Peralta, F. Ogliaro, M. Bearpark, J. J. Heyd, E. Brothers, K. N. Kudin, V. N. Staroverov, R. Kobayashi, J. Normand, K. Raghavachari, A. Rendell, J. C. Burant, S. S. Iyengar, J. Tomasi, M. Cossi, N. Rega, J. M. Millam, M. Klene, J. E. Knox, J. B. Cross, V. Bakken,

C. Adamo, J. Jaramillo, R. Gomperts, R. E. Stratmann, O. Yazyev, A. J. Austin, R. Cammi, C. Pomelli, J. W. Ochterski, R. L. Martin, K. Morokuma, V. G. Zakrzewski, G. A. Voth, P. Salvador, J. J. Dannenberg, S. Dapprich, A. D. Daniels, O. Farkas, J. B. Foresman, J. V. Ortiz, J. Cioslowski, and D. J. Fox, Gaussian, Inc., Wallingford CT, **2009**.

[2] T. Lu, F. Chen, *J. Mol. Graph. Model.* **2012**, *38*, 314–323.

[3] J. B. Maglic, R. Lavendomme, *J. Appl. Cryst*. **2022**, *55*, 1033–1044.

[4] K. Rissanen, *Chem. Soc. Rev.* **2017**, *46*, 2638–2648.

[5] C. G. P. Taylor, S. P. Argent, M. D. Ludden, J. R. Piper, C. Mozaceanu, S. A. Barnett, M. D. Ward, *Chem. Eur. J*. **2020**, *26*, 3054–3064.

[6] P. Thordarson, *Chem. Soc. Rev.* **2011**, *40*, 1305–1323.